

Actively tuning anisotropic light-matter interaction in biaxial hyperbolic material α-MoO_3 using phase change material VO_2 and graphene

Kun Zhou(周昆), Yang Hu(胡杨), Biyuan Wu(吴必园), Xiaoxing Zhong(仲晓星), and Xiaohu Wu(吴小虎)

Citation: Chin. Phys. B, 2024, 33 (**4**): 047103. DOI: 10.1088/1674-1056/ad23d2
Journal homepage: http://cpb.iphy.ac.cn; http://iopscience.iop.org/cpb

What follows is a list of articles you may be interested in

Effects of vacancy and external electric field on the electronic properties of the $MoSi_2N_4$/graphene heterostructure

Qian Liang(梁前), Xiangyan Luo(罗祥燕), Guolin Qian(钱国林), Yuanfan Wang(王远帆), Yongchao Liang(梁永超), and Quan Xie(谢泉)

Chin. Phys. B, 2024, 33 (**3**): 037101. DOI: 10.1088/1674-1056/acef04

Atomistic simulations of graphene origami: Dynamics and kinetics

Panpan Zhang(张盼盼), Haihong Jia(贾海洪), Yan-Fang Zhang(张艳芳), and Shixuan Du(杜世萱)

Chin. Phys. B, 2023, 32 (**8**): 087107. DOI: 10.1088/1674-1056/acd527

Rashba spin-orbit coupling induced rectified currents in monolayer graphene with exchange field and sublattice potential

Liang Chen(陈亮), Feng Li(李峰), and Xiao-Ming Ding(丁晓明)

Chin. Phys. B, 2023, 32 (**8**): 087103. DOI: 10.1088/1674-1056/acc932

Thermal spin molecular logic gates modulated by an electric field

Xingyi Tan(谭兴毅), Qiang Li(李强), and Dahua Ren(任达华)

Chin. Phys. B, 2023, 32 (**5**): 057101. DOI: 10.1088/1674-1056/ac89e5

Modulation of Schottky barrier in XSi_2N_4/graphene (X=Mo and W) heterojunctions by biaxial strain

Qian Liang(梁前), Xiang-Yan Luo(罗祥燕), Yi-Xin Wang(王熠欣), Yong-Chao Liang(梁永超), and Quan Xie(谢泉)

Chin. Phys. B, 2022, 31 (**8**): 087101. DOI: 10.1088/1674-1056/ac5c3b

---

Actively tuning anisotropic light–matter interaction in biaxial hyperbolic material α-MoO_3 using phase change material VO_2 and graphene

Kun Zhou(周昆)[1,2], Yang Hu(胡杨)[3,4], Biyuan Wu(吴必园)[3,4], Xiaoxing Zhong(仲晓星)[1,2,†], and Xiaohu Wu(吴小虎)[3,‡]

[1] *School of Safety Engineering, China University of Mining and Technology, Xuzhou* 221116, *China*
[2] *Key Laboratory of Gas and Fire Control for Coal Mines (Ministry of Education), China University of Mining and Technology, Xuzhou* 221116, *China*
[3] *Shandong Institute of Advanced Technology, Jinan* 250100, *China*
[4] *School of Power and Energy, Northwestern Polytechnical University, Xi'an* 710072, *China*

(Received 11 September 2023; revised manuscript received 10 January 2024; accepted manuscript online 30 January 2024)

Anisotropic hyperbolic phonon polaritons (PhPs) in natural biaxial hyperbolic material α-MoO_3 has opened up new avenues for mid-infrared nanophotonics, while active tunability of α-MoO_3 PhPs is still an urgent problem necessarily to be solved. In this study, we present a theoretical demonstration of actively tuning α-MoO_3 PhPs using phase change material VO_2 and graphene. It is observed that α-MoO_3 PhPs are greatly dependent on the propagation plane angle of PhPs. The insulator-to-metal phase transition of VO_2 has a significant effect on the hybridization PhPs of the α-MoO_3/VO_2 structure and allows to obtain actively tunable α-MoO_3 PhPs, which is especially obvious when the propagation plane angle of PhPs is 90°. Moreover, when graphene surface plasmon sources are placed at the top or bottom of α-MoO_3 in α-MoO_3/VO_2 structure, tunable coupled hyperbolic plasmon–phonon polaritons inside its Reststrahlen bands (RBs) and surface plasmon–phonon polaritons outside its RBs can be achieved. In addition, the above-mentioned α-MoO_3-based structures also lead to actively tunable anisotropic spontaneous emission (SE) enhancement. This study may be beneficial for realization of active tunability of both PhPs and SE of α-MoO_3, and facilitate a deeper understanding of the mechanisms of anisotropic light–matter interaction in α-MoO_3 using functional materials.

Keywords: light–matter interaction, hyperbolic material, phase change material, graphene

PACS: 71.36.+c, 63.22.Rc, 63.20.D– **DOI:** 10.1088/1674-1056/ad23d2

1. Introduction

Hyperbolic materials (HMs) exhibit unique optical, electronic and magnetic properties, their natural hyperbolicity offers advantages over other conventional metal and dielectric materials.[1–6] As a special class of HMs, biaxial α-phase molybdenum trioxide (α-MoO_3) has drawn much attention due to its enigmatic optoelectronic characteristics throughout the infrared regions.[7–9] So far, α-MoO_3 composing of octahedral unit cells with nonequivalent Mo–O bonds along its three principal crystalline axes (between 550 cm^{-1} and 1000 cm^{-1}) has attracted huge attention owing to its ability to excite highly anisotropic phonon polaritons (PhPs) with in-plane hyperbolic and elliptic dispersion,[10] which gives rise to a versatile platform for studying anisotropic light–matter interaction. Because of its biaxial anisotropy and hyperbolicity, α-MoO_3 is an excellent candidate to provide more rich physical phenomena than other HMs, thus an in-depth understanding of α-MoO_3 is greatly significant for many different fields involving light–matter interactions, such as near-field radiative heat transfer, super-resolution technologies, spontaneous emission (SE) and spectral absorption.[11–14] However, the active tunability of PhPs excited by resonance between photons and α-MoO_3 is still a challenge owing to their inherent crystal lattice resulting in inefficient tunability.

Stacking and combining functional materials into a heterostructure offers a flexible and promising way to couple material properties and reveal underlying physical phenomena.[15,16] As a typical functional material, because of its electrostatic doping possibility and ability to generate higher confinement and lower losses,[15,16] graphene becomes an excellent candidate for the realization of tunable surface plasmon polaritons (SPPs) via applying extra gate voltage in the mid-infrared and terahertz frequency ranges.[17–19] Meanwhile, graphene can be flexibly combined with other micro/nanostructures and HMs to obtain coupled hybridization characteristics, which provides an alternative route to realize tunable optoelectronic devices.[20,21] Over the past few years, graphene has been applied to realize tunable hyperbolic plasmon–phonon dispersion, near-field radiative heat transfer, SE enhancement and spectral absorption.[22–26] Except for graphene, phase-change materials (PCMs) including $Ge_2Sb_2Te_5$ (GST) and vanadium dioxide (VO_2) have witnessed abundant achievements toward actively tunable light–matter interaction from the perspectives of principles and applications.[15,16,27] Compared to that from amorphous GST

†Corresponding author. E-mail: zhxxcumt@cumt.edu.cn
‡Corresponding author. E-mail: xiaohu.wu@iat.cn

© 2024 Chinese Physical Society and IOP Publishing Ltd

to crystalline GST at about 438 K,[16] the phase-transition temperature of VO_2 from insulator to metal is about 340 K,[28] which is easy to achieve and has little influence on the corresponding cooperating materials. Meanwhile, the phase-transition temperature of VO_2 can be tuned by doping VO_2 flake with W, Ti, Mg, and Al nanoparticles forming $M_xV_{1-x}O_2$ (M = W, Ti, Mg, or Al),[29–33] such as the transition temperature can be tailored to 295 K by setting the composition x at 1.5% in $W_xV_{1-x}O_2$.[33] Because its advantages over other PCMs, VO_2 serves as the basis for potential applications such as temperature-adaptive radiative coating, energy storage and reconfigurable electronics.[34,35]

Since the dispersion modes including phonons and plasmons can be tuned in layered van der Waals material systems using functional materials,[15,16] in this study, a theoretical platform is proposed to realize anisotropic light–matter interaction in α-MoO_3 by using phase transition properties of VO_2 and SPPs of graphene. Hybridization PhP dispersion modes of α-MoO_3 and coupling hybridization dispersion between α-MoO_3 PhPs and graphene SPPs based on VO_2 substrate will be detailedly discussed, meanwhile the propagation plane angle in biaxial α-MoO_3 will also be considered. Furthermore, comparative analysis of actively tunable anisotropic SE enhancement in α-MoO_3-based structures will also be investigated.

2. The geometry and numerical model

In order to actively tune and control PhPs behavior of the biaxial HM α-MoO_3 along its main crystallographic directions, a VO_2 layer is used as the substrate owing to its attractive dielectric properties during the temperature-tuned insulator-to-metal phase transition, and the complex refractive index of VO_2 is refereed from Ref. [29]. The above-mentioned schematic is displayed in Fig. 1(a), where a Cartesian coordinate system is established, x, y and z axes represent the [100], [001] and [010] crystal directions of the α-MoO_3, respectively; ϕ is the propagation plane angle of PhPs with respect to the [100] crystal direction, t is defined as the α-MoO_3 thickness. Here α-MoO_3 is a natural biaxial HM and its optical response is dominated by the phonon absorption, whose principal permittivity components can be expressed as the following Lorentz equation:[9]

$$\varepsilon_j = \varepsilon_\infty^j\left(1+\frac{\omega_{\mathrm{LO}}^{j2}-\omega_{\mathrm{TO}}^{j2}}{\omega_{\mathrm{TO}}^{j2}-\omega^2-\mathrm{i}\omega\Gamma^j}\right), \tag{1}$$

where $j = x, y, z$ denotes the three crystal principal axes, corresponding to the crystalline directions [100], [001] and [010] of α-MoO_3, respectively; ε_∞^j represents the high-frequency dielectric constant; ω_{LO}^j and ω_{TO}^j refer to the longitudinal and transverse optical phonon frequencies; Γ^j is the broadening factor of the Lorentzian line shape, and the corresponding parameters can be referred from Ref. [9].

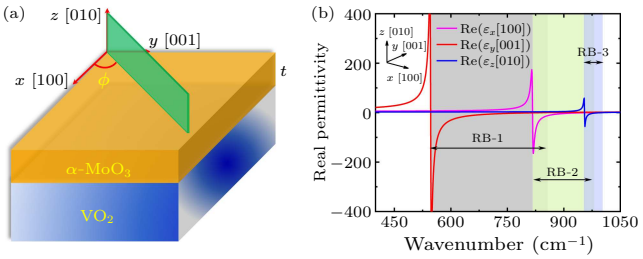


Fig. 1. (a) Schematic illustration of the α-MoO_3/VO_2 structure. (b) Real parts of the principal permittivity tensor components of α-MoO_3.

The real parts of the dielectric tensor components ε_j in α-MoO_3 are displayed in Fig. 1(b), three Reststrahlen bands (RBs) exist in the mid-infrared range from 545 cm^{-1} to 1010 cm^{-1}. RB-1, RB-2 and RB-3 of α-MoO_3 are respectively in the ranges from 545 cm^{-1} to 851 cm^{-1} (the gray region), from 820 cm^{-1} to 972 cm^{-1} (the green region) and from 958 cm^{-1} to 1010 cm^{-1} (the purple region), which originate from in-plane phonon modes along the [001], [100] and [010] crystalline directions, respectively. It is worth noting that RB-1 and RB-2 belong to the type-II hyperbolic band, while RB-3 to the type-I hyperbolic band. In addition, the relative permittivity tensor of α-MoO_3 for the propagation angle ϕ is obtained from $\varepsilon(\phi) = R(\phi)\varepsilon_{\alpha\text{-}\mathrm{MoO_3}}R^{\mathrm{T}}(\phi)$, where $R(\phi)$ is the rotation matrix for transformation of coordinate system, and the relative permittivity tensor of α-MoO_3 can be written as[36,37]

$$\varepsilon(\phi) = \begin{pmatrix} \varepsilon_x\cos^2\phi+\varepsilon_y\sin^2\phi & \sin\phi\cos\phi(\varepsilon_y-\varepsilon_x) & 0 \\ \sin\phi\cos\phi(\varepsilon_y-\varepsilon_x) & \varepsilon_x\sin^2\phi+\varepsilon_y\cos^2\phi & 0 \\ 0 & 0 & \varepsilon_z \end{pmatrix}. \tag{2}$$

Since graphene supports SPPs in the mid-infrared region, graphene layers are added at the top or bottom of α-MoO_3 layer to realize additional PhPs tunability of the α-MoO_3 and investigate coupling hybridization dispersion between α-MoO_3 PhPs and graphene SPPs. In this study, graphene is treated as an ultrathin dielectric layer with the thickness Δ = 0.34 nm by an effective permittivity $\varepsilon = 1+\mathrm{i}\sigma_{\mathrm{g}}/(\omega\varepsilon_0\Delta)$,[24] ε_0 is vacuum permittivity, and its conductivity σ_{g} modeled as a sum of the intraband and interband terms is given by $\sigma_{\mathrm{g}} = \sigma_{\mathrm{intra}}+\sigma_{\mathrm{inter}}$ written as[24]

$$\sigma_{\mathrm{intra}} = \frac{\mathrm{i}}{\omega+\frac{\mathrm{i}}{\tau_{\mathrm{g}}}}\frac{2e^2k_{\mathrm{B}}T}{\pi\hbar^2}\ln\left[2\cos\left(\frac{\mu_{\mathrm{g}}}{2k_{\mathrm{B}}T}\right)\right], \tag{3}$$

$$\sigma_{\mathrm{inter}} = \frac{e^2}{4\hbar}\left[G\left(\frac{\hbar\omega}{2}\right)+\frac{4\mathrm{i}\hbar\omega}{\pi}\int_0^\infty\frac{G(\xi)-G(\frac{\hbar\omega}{2})}{(\hbar\omega)^2-4\xi^2}\mathrm{d}\xi\right], \tag{4}$$

where $G(\xi) = \sinh(\xi/k_{\mathrm{B}}T)/[\cosh(\mu_{\mathrm{g}}/k_{\mathrm{B}}T)+\cosh(\xi/k_{\mathrm{B}}T)]$; τ_{g}, e, k_{B}, μ_{g}, $\hbar$ and T are the relaxation scattering time, electron charge, Boltzmann constant, chemical potential, reduced Planck's constant, and temperature, respectively.

3. Results and discussion

3.1. Actively tuning biaxial PhPs of α-MoO_3 based on VO_2 substrate

The dispersion relations of the above-mentioned heterostructures are calculated by an intensity of the imaginary part of the Fresnel reflection coefficient $\mathrm{Im}(r^{pp})$,[15,16] where r^{pp} is the Fresnel reflection coefficient for p-polarized wave, which is calculated using the 4×4 matrix[38–40] $\mathbb{R} = \begin{pmatrix} r^{ss} & r^{sp} \\ r^{ps} & r^{pp} \end{pmatrix}$. Meanwhile, the whole results are calculated by using the MATLAB. As shown in Fig. 2, the hybridization PhP dispersion of the α-MoO_3/VO_2 structure along its main crystallographic directions at the metal- and insulator-state of VO_2 are calculated. Meanwhile, since α-MoO_3 is a biaxial HM, the effects of the propagation plane angle ϕ on the PhP dispersion modes of α-MoO_3 are also considered at $\phi = 0°$, $\phi = 45°$ and $\phi = 90°$, respectively. The thickness of the α-MoO_3 layer is 150 nm to ignore the quantum confinement effects.[9] It is worth noting that the color bars of the hybridization dispersion modes are appropriately adjusted to clearly show the differences. When VO_2 is in the metal state shown in Figs. 2(a)–2(c), two hybridization PhP dispersion modes of the α-MoO_3/VO_2(I) structure at $\phi = 0°$ are gathering inside RB-2 and RB-3, and the dispersion modes lead to group velocity $v_g = \mathrm{d}w/\mathrm{d}g > 0$[16] in RB-2 and $v_g < 0$ in RB-3, respectively. Two PhP dispersion modes of the α-MoO_3/VO_2(I) structure at $\phi = 90°$ occur at RB-1 and RB-3, the group velocity in RB-2 keeps the same sign as that at $\phi = 0°$, meanwhile the group velocity is $v_g > 0$ in RB-1. Interestingly, PhP dispersions of the α-MoO_3/VO_2(I) structure at $\phi = 45°$ occur simultaneously within its three RBs and just span the part frequency range of its RBs. Moreover, with the increase of the propagation plane angles from $\phi = 0°$ to $\phi = 90°$, PhP dispersions of the α-MoO_3/VO_2 structure within RB-3 always exist because of the contribution of permittivity tensor along [010] crystalline directions, while PhP dispersions of the α-MoO_3/VO_2 structure within RB-1 gradually widen to nearly 851 cm^{-1} and within RB-2 gradually narrow to disappear, which are attributed to the overall consideration of the rotated permittivity tensor between [100] and [001] crystalline directions.[36,37] In addition, similar results can also be obtained when VO_2 is in the insulator state shown in Figs. 2(d)–2(f), while the hybridization PhP dispersion modes of α-MoO_3 are different before and after VO_2 phase transition, and the results about the adjustment resulting from bottom VO_2 are considered from the whole structure. Regardless of the phase transition state of VO_2, the hybridization PhP dispersion modes in α-MoO_3 exhibit obviously in-plane anisotropic behaviors.

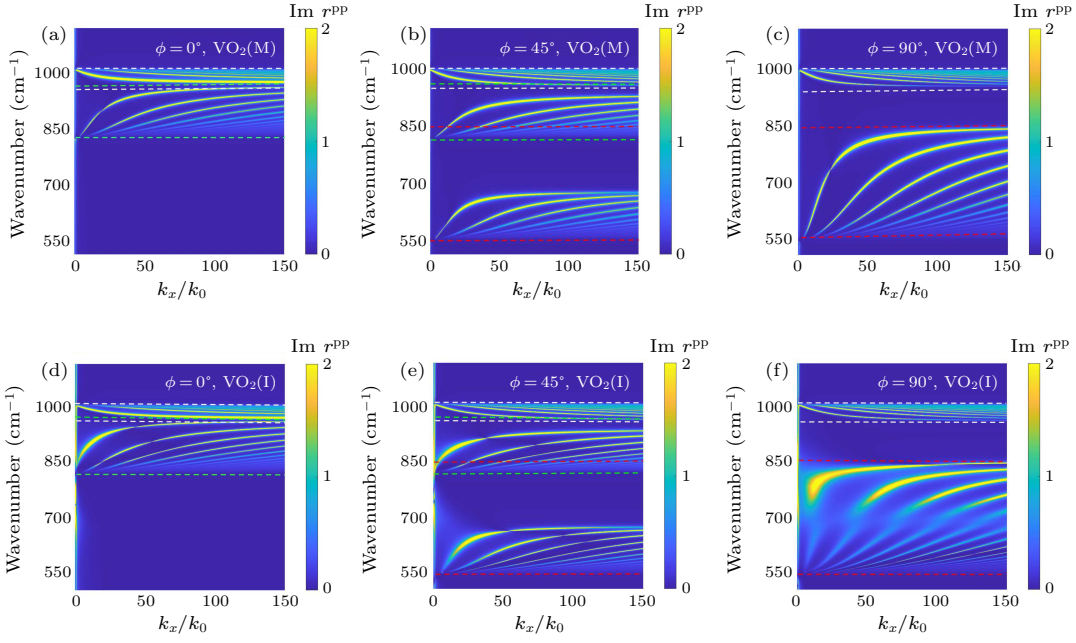


Fig. 2. Hybridization dispersions of the α-MoO_3/VO_2 structure for different propagation plane angles ϕ at (a)–(c) metal state and (d)–(f) insulator state of VO_2. The dashed lines of different colors represent the intrinsic RBs of α-MoO_3.

As an example, hybridization PhP dispersion modes of the α-MoO_3/VO_2(M) and α-MoO_3/VO_2(I) structures at $\phi = 90°$ are analyzed, as shown in Figs. 2(c) and 2(f). Since the insulator-to-metal transition has a profound impact on the dielectric properties of VO_2, compared to that in the α-MoO_3/VO_2(M) structure, the hybridization PhP branches in the α-MoO_3/VO_2(I) structure significantly approach to the light line and widen, which can be attributed to its inherent lossy enhancement of VO_2 once it undergoes a phase transition from the insulator state to metal state. Furthermore, in order to clearly describe that VO_2 can actively tune α-MoO_3 PhPs, hybridization PhP dispersions of the α-MoO_3/VO_2(M)

and α-MoO_3/VO_2(I) structures varying with the wavevector components k_x and k_y at the wavenumber of 780 cm^{-1} are calculated as shown in Figs. 3(a) and 3(b). The excitation range of hybridization PhP dispersion branches reads $-\sqrt{-\varepsilon_x/\varepsilon_y} < k_y/k_x < \sqrt{-\varepsilon_x/\varepsilon_y}$,[41] the corresponding dielectric function components of α-MoO_3 at the wavenumber of 780 cm^{-1} are $\varepsilon_x = 20.7 - i0.8$ and $\varepsilon_y = -1.95 - i0.07$. As shown in Figs. 3(a) and 3(b), the bright color within the regions up and down the origin being bounded by the two white dashed lines of $k_y \approx \pm 3.26 k_x$ is of the hybridization PhP dispersion branches. Once VO_2 undergoes a insulator-to-metal phase transition at the wavenumber of 780 cm^{-1}, the complex dielectric function of VO_2 will convert from $\varepsilon_{VO_2(I)} = 0.72 + i0.96$ to $\varepsilon_{VO_2(M)} = -10.91 + i103.48$, thus the dielectric function differences of VO_2 between metal state and insulator state leading to the hybridization PhP dispersion modes in the α-MoO_3/VO_2 structure are different, and its hybridization PhP dispersion branches gradually move towards to the directions of a smaller vector. Furthermore, the analytical expression for the dispersion relations of the α-MoO_3/VO_2 structure under the quasistatic approximation is utilized and can be written as[12]

$$\frac{k_\rho}{k_0} = \frac{\xi}{k_0 t}\left[\arctan\left(\frac{\varepsilon_1 \xi}{\varepsilon_z}\right) + \arctan\left(\frac{\varepsilon_{VO_2}\xi}{\varepsilon_z}\right) + l\pi\right], \quad l = 0, 1, 2, \ldots, \tag{5}$$

where ε_1 and ε_{VO_2} are the permittivities of air and VO_2, t is the α-MoO_3 flake thickness, ε_z is the α-MoO_3 permittivity along the [010] crystalline directions, and $\xi = i\sqrt{\varepsilon_z/(\varepsilon_x \cos^2\phi + \varepsilon_y \sin^2\phi)}$. As shown in Figs. 3(a) and 3(b), the hybridization PhP dispersion branches of the α-MoO_3/VO_2 structure with green dashed lines agree well with those using the 4×4 matrix.

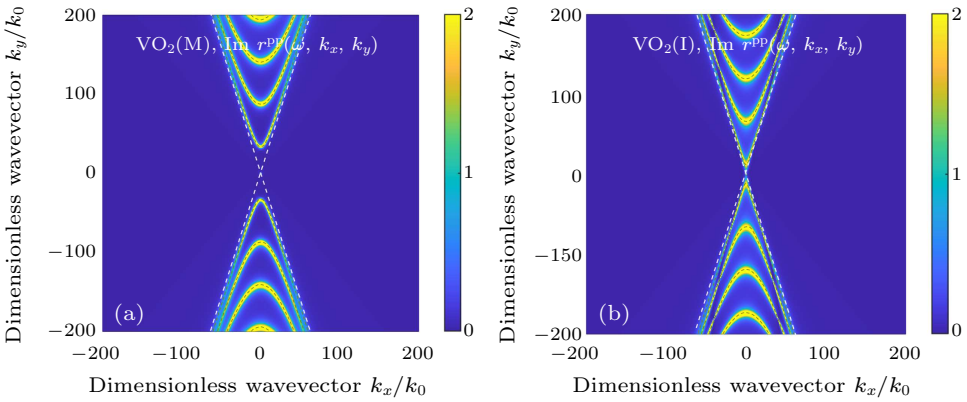


Fig. 3. Hybridization dispersions of (a) α-MoO_3/VO_2(M) and (b) α-MoO_3/VO_2(I) structures varying with wavevector components k_x and k_y at the wavenumber of 780 cm^{-1}.

3.2. Coupling hybridization dispersion between α-MoO_3 PhPs and graphene SPPs

The previous study clarified that active tunability of α-MoO_3 PhPs can be achieved through the phase transition of VO_2 without changing the structural parameters. Since graphene supports SPPs in the mid-infrared and terahertz region,[18,19] which provides a flexible way to investigate coupling hybridization dispersion modes in α-MoO_3, two heterostructures are proposed to realize coupling hybridization dispersion between α-MoO_3 PhPs and graphene SPPs. As a benchmark, a graphene layer is added on the top of the α-MoO_3/VO_2 structure as shown in Fig. 4(g) and its hybridization dispersion modes will be investigated. Here, $\mu_g = 0.3$ eV is chosen and fixed to investigate coupling hybridization dispersion modes, using other graphene chemical potentials can also obtain similar conclusions, and the results are not shown here. At $\phi = 0°$ shown in Figs. 4(a) and 4(d), coupling hybridization hyperbolic plasmon-phonon polariton (HPPP) dispersion modes between α-MoO_3 PhPs and graphene SPPs occur within its RBs,[42] which are not pure PhPs displayed in Figs. 2(a) and 2(d) of the α-MoO_3/VO_2 structure. Especially within RB-2, the coupling hybridization polariton branches in α-MoO_3 are broader and move closer to the light cone because of the inherently lossy of the graphene SPPs, and the group velocity obviously increases when compared with that of the α-MoO_3/VO_2 structure in Figs. 2(a) and 2(d). Compared to the hybridization dispersion in the α-MoO_3/VO_2 structure, outside its RBs, surface plasmon-phonon polaritons (SPPPs) are formed by coupling with α-MoO_3 PhPs through the dominant contribution of graphene SPPs, and possess positive group velocity keeping similar with graphene SPPs.[42] Similar results can also be obtained at $\phi = 45°$ [Figs. 4(b) and 4(e)] and $\phi = 90°$ [Figs. 4(c) and 4(f)]. It is worth noting that increasing the graphene chemical potential in the graphene/α-MoO_3/VO_2 structure, coupling hybridization dispersion branches gradually shift to the direction of the light line and the characteristics of graphene SPPs in the coupled hybridization dispersion become more obvious, which can be attributed to the strong coupling between α-MoO_3 PhPs and graphene SPPs. In addition, changing the phase transition state of VO_2 can also actively tune both coupled HPPP and

SPPP dispersion modes in the graphene/α-MoO_3/VO_2 structure without changing the structural parameters.

Based on the graphene/α-MoO_3/VO_2 structure, an additional heterostructure with the placement of a surface plasmon source on either side of the α-MoO_3 is considered to further investigate both HPPP and SPPP dispersion modes, as schematically shown in Fig. 5(g). Figures 5(a)–5(f) show the hybridization dispersion modes of the graphene/α-MoO_3/graphene/VO_2 structure, here keeping $\mu_{g1} = \mu_{g2} = 0.3$ eV unchanged for simplicity. Compared with that in graphene/α-MoO_3/VO_2 structure, the coupling effect is even more pronounced via the extra contribution of the graphene SPPs at the bottom of the α-MoO_3 layer. When compared with that of the VO_2 substrate in insulator state shown in Figs. 5(a)–5(c), the hybridization dispersion modes of the graphene/α-MoO_3/graphene/VO_2(M) structure shown in Figs. 5(d)–5(f) obviously move closer to the light cone and widen, especially for $\phi = 90°$ displayed in Fig. 5(f), which can be attributed to the reflection reinforcement at the VO_2 layer once it changes from insulator state to metal state.[15]

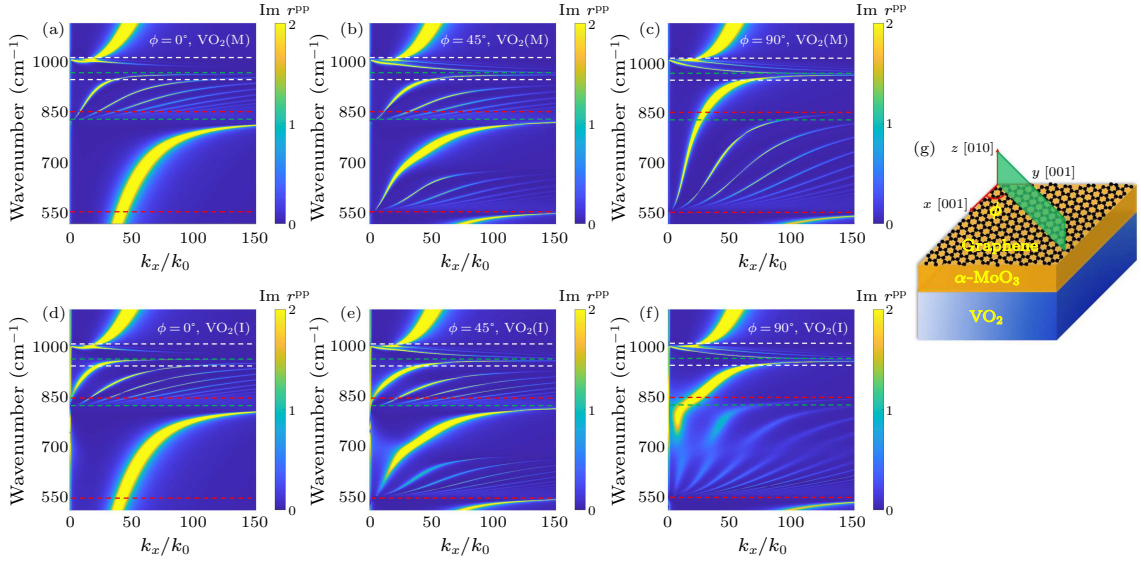


Fig. 4. Hybridization dispersions of the graphene/α-MoO_3/VO_2 structure at (a)–(c) metal state and (d)–(f) insulator state of VO_2 for different propagation plane angles ϕ. (g) Schematic illustration of the graphene/α-MoO_3/VO_2 structure. The dashed lines of different colors represent the intrinsic RBs of α-MoO_3.

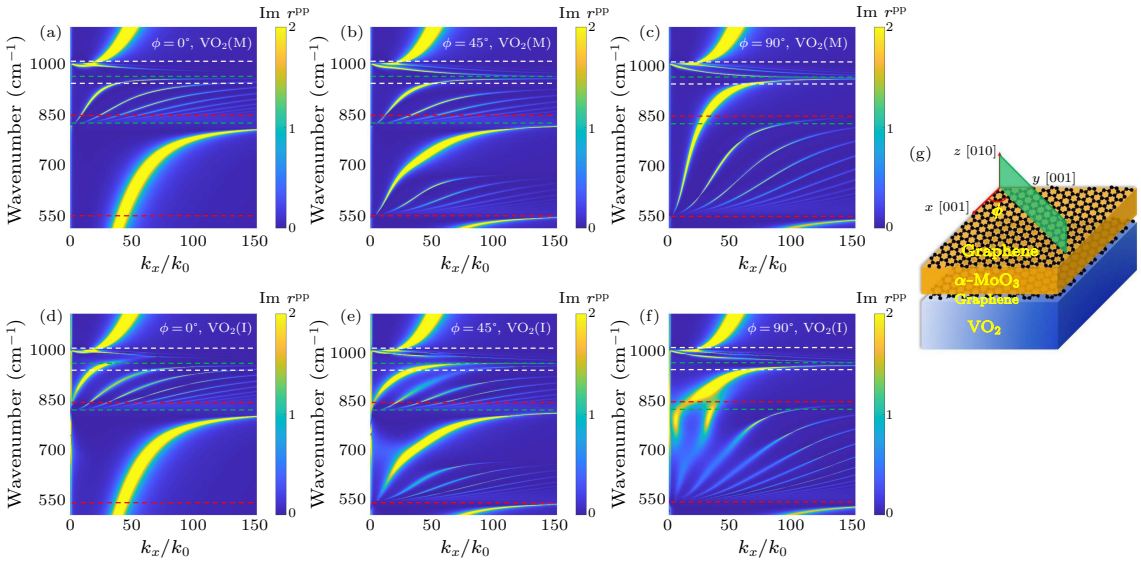


Fig. 5. Hybridization dispersions of the graphene/α-MoO_3/graphene/VO_2 structure at (a)–(c) metal state and (d)–(f) insulator state of VO_2 for different propagation plane angles ϕ. (g) Schematic of the graphene/α-MoO_3/graphene/VO_2 structure. The dashed lines of different colors represent the intrinsic RBs of α-MoO_3.

Furthermore, the hybridization dispersion modes of the graphene/α-MoO_3/VO_2 and graphene/α-MoO_3/graphene/VO_2 structures varying with the wavevector components k_x and k_y at the wavenumber 780 cm^{-1} are also calculated in Figs. 6(a)–6(d) to illustrate the differences. Coupling hybridization HPPP dispersion modes occur within the asymptotes $k_y \approx +3.26k_x$ and $k_y \approx -3.26k_x$, and coupling hybridization SPPP dispersion modes appearing

on the left and right sides of the origin are mainly derived from the contribution of graphene SPPs. When VO_2 in the graphene/α-MoO_3/VO_2 structure experiences the insulator-to-metal phase transition, its hybridization HPPP dispersion branches on the top and bottom sides of the origin gradually move towards the direction of zero-wave vector. Furthermore, as another graphene layer is added at the bottom of α-MoO_3 layer in the graphene/α-MoO_3/VO_2 structure shown in Figs. 6(c)–6(d), coupling hybridization dispersion modes between α-MoO_3 PhPs and graphene SPPs are stronger, and hybridization HPPP dispersion branches obviously move towards to the origin.

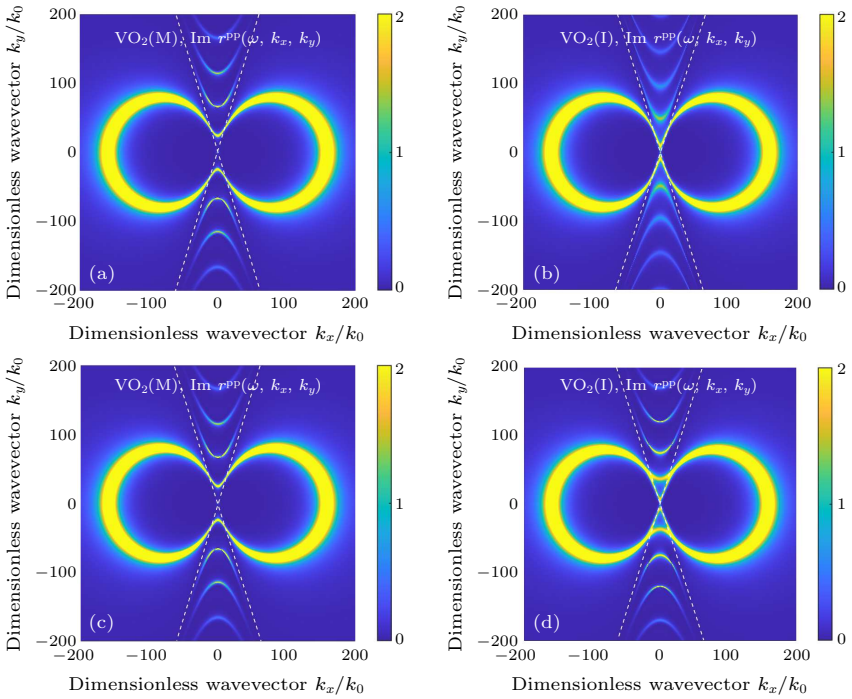


Fig. 6. Hybridization dispersions of [(a), (b)] graphene/$\alpha-MoO_3/VO_2$ and [(c), (d)] graphene/α-MoO_3/graphene/VO_2 structures varying with wavevector components k_x and k_y at the wavenumber of 780 cm^{-1}.

3.3. Actively tuning anisotropic SE enhancement in α-MoO_3-based structures

In this section, we present a comparative analysis of anisotropic SE enhancement in α-MoO_3-based structures to illustrate the VO_2 phase change so as to realize actively tunable SE. As compared with that in free space, the lifetime of an excited quantum emitter being placed near a special photonic material system can be modified, which is called Purcell effect.[43] Hybridization dispersion mode modulated interaction with graphene and α-MoO_3 on VO_2 substrate has significant effects on the SE rate of an excited quantum emitter. When the moment of the dipole on a system is along the z-direction, its SE rate (Purcell spectrum) can be described as[44]

$$\frac{\Gamma}{\Gamma_0} = 1 + \frac{3}{2k_0^3}\mathrm{Re}\left[\int_0^\infty \frac{r^{\mathrm{pp}}(\omega,k_x)\,\mathrm{e}^{2\mathrm{i}k_z d_\mathrm{s}}k_x^3\,\mathrm{d}k_x}{k_z}\right], \tag{6}$$

where Γ and $\Gamma_0 = \omega_0^3|p_z|^2/3\pi\varepsilon_0\hbar c^3$ are the SE rate of a dipole emitter near the system and in free space, d_s is the distance between the dipole emitter and proposed systems, $r^{\mathrm{pp}}(\omega,k_x)$ is the total Fresnel reflection coefficient of the proposed systems.[38,39]

Then, the SE rates of α-MoO_3-based structure are investigated and discussed. The effects of the geometric parameters on the SE rates of the α-MoO_3/VO_2 structure are firstly discussed in Fig. 7, the basic geometrical parameters are set as $d_\mathrm{s} = 100$ nm, $t = 150$ nm, and $\phi = 0°$. As shown in Figs. 7(a) and 7(b), with the increasing d_s from 80 nm to 120 nm, the SE rates of the α-MoO_3/VO_2 structure obviously reduce, which indicates that the SE rates is inversely proportional to the distance d_s.[23,45,46] Results in Figs. 7(c) and 7(d) show that the SE rates of the α-MoO_3/VO_2 structure keep the same order with the increasing α-MoO_3 thickness t from 50 nm to 200 nm. Then, the effects of the propagation plane angle ϕ on the SE rates of the α-MoO_3/VO_2 structure are also discussed in Figs. 7(e) and 7(f), the enhancement regions of SE rate mainly gather within its hyperbolic bands, with increasing the propagation plane angle ϕ from 0 to 90°, the SE enhancements within RB-3 always exist, while the SE enhancements at RB-1 and RB-2 greatly rely on propagation plane angle ϕ, which can be attributed to the contribution of α-MoO_3 PhPs. The above discussion indicates the SE enhancements mainly rely on the distance d_s and the propagation plane angle ϕ. Moreover, results in Fig. 7 indicate the SE rate of the α-MoO_3/VO_2 structure significantly change as the VO_2 substrate undergoes the insulator-to-metal phase transition, which provides a feasible way to actively tune the SE rates of the α-MoO_3.

Since the conductivity of graphene can be modulated by applying an extra gate voltage, which is an advantage for using graphene for photonics applications. Subsequently, SE rates of the graphene/α-MoO_3/VO_2 structure are theoretically investigated, as shown in Figs. 8(a) and 8(b). The SE rates of the graphene/α-MoO_3/VO_2 structure keep similar characteristics with those in α-MoO_3/VO_2 structure, meanwhile the ratio of SE rate of the α-MoO_3/VO_2 structure with and without adding different graphene layers is introduced for evaluating the tuning performance, which is defined as

$$\text{Ratio} = \frac{\text{SE rate of the structure with graphene}}{\text{SE rate of the structure without graphene}}.$$

Figures 8(c) and 8(d) give the ratio of SE rate of the α-MoO_3/VO_2 system with and without adding graphene layers. When compared to SE rates of the α-MoO_3/VO_2 structure, SE rates with adding graphene layers obvious enhance outside the RBs and are independent of the propagation plane angle ϕ, which can be attributed to the contribution of the SPPPs. While SE rates within the RBs are mainly caused by the strong coupling between graphene plasmons and α-MoO_3 phonon polaritons, its enhancement is dependent on the propagation plane angle ϕ. In addition, SE rates of the graphene/α-MoO_3/graphene/VO_2 structure are also considered, as shown in Figs. 8(e)–8(h), except for the magnitude, its SE rates are basically the same as those in the graphene/α-MoO_3/VO_2 structure, thus the graphene layer at the bottom of the α-MoO_3 layer in the graphene/α-MoO_3/VO_2 structure just plays a role in adding flexibility. When comparing the proposed α-MoO_3-based structures, the α-MoO_3/VO_2 structure is easy to realize, while the graphene/α-MoO_3/VO_2 and graphene/α-MoO_3/graphene/VO_2 structures can provide richer physical modes.

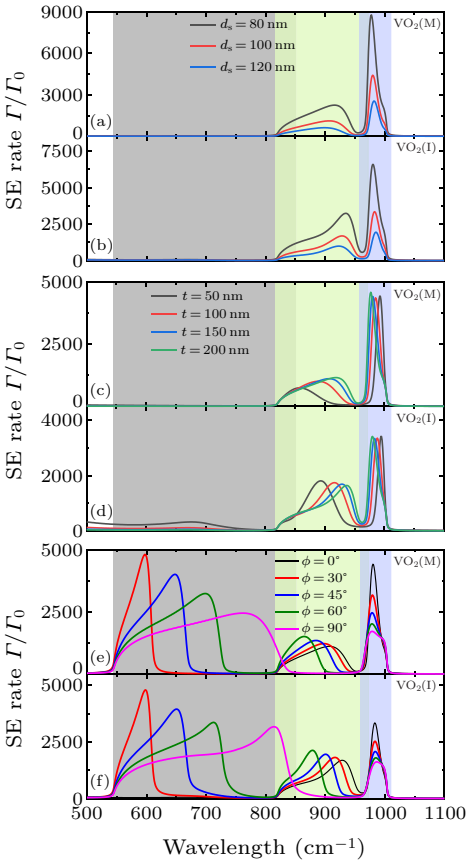


Fig. 7. The effects of the geometric parameters on the SE rates of the α-MoO_3/VO_2 structure, [(a), (b)] the distance d_s, [(c), (d)] the α-MoO_3 thickness t, [(e), (f)] the propagation plane angle ϕ, keeping the other geometric parameters $d_s = 100$ nm, $t = 150$ nm, and $\phi = 0°$ unchanged.

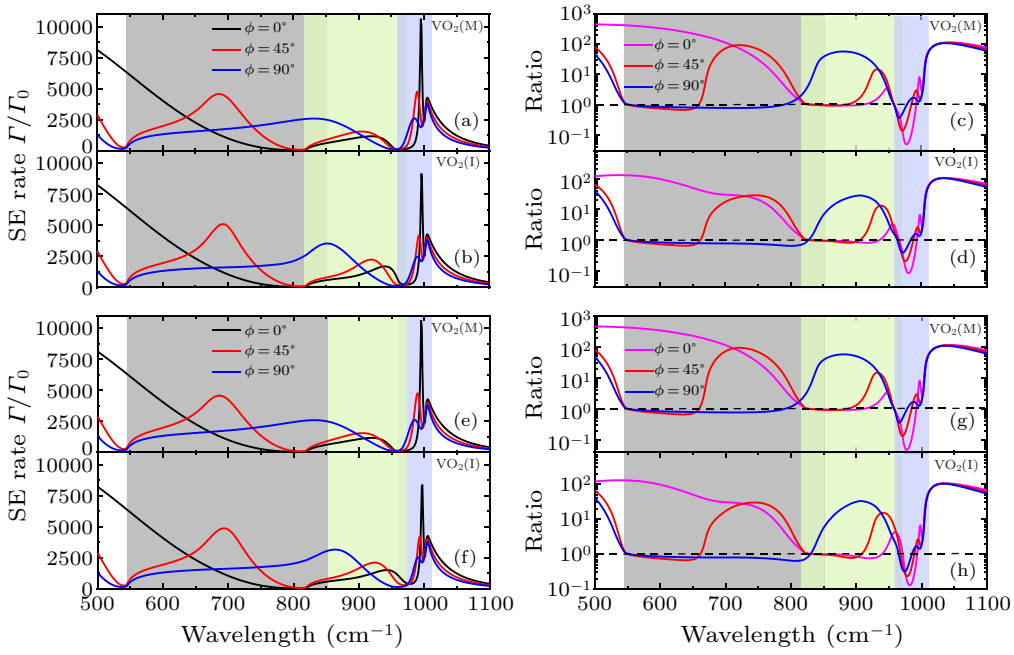


Fig. 8. SE rates and the ratio of SE rate of the α-MoO_3/VO_2 structure with and without adding graphene layers: (a)–(d) graphene/α-MoO_3/VO_2 structure, (e)–(h) graphene/α-MoO_3/graphene/VO_2 structure, with $d_s = 100$ nm, $t = 150$ nm, $\mu_g = 0.3$ eV.

4. Conclusion

In summary, a theoretical platform is proposed to actively tune anisotropic light–matter interaction in biaxial HM α-MoO_3 using phase change material VO_2 and graphene. For the α-MoO_3/VO_2 structure, the hybridization PhP dispersion modes in α-MoO_3 exhibit obvious in-plane anisotropic behaviors, and the hybridization PhPs in α-MoO_3 are greatly dependent on propagation plane angle, its hybridization PhP dispersion modes are gathering inside RB-2 and RB-3 at $\phi = 0°$ and RB-1 and RB-3 at $\phi = 90°$, while its hybridization PhP dispersion modes simultaneously occur in all RBs and just span the part frequency range of RBs at $\phi = 45°$. Meanwhile, the insulator-to-metal phase transition of VO_2 has a significant effect on the hybridization PhPs of α-MoO_3/VO_2 structure, and allows to realize an active tunable α-MoO_3 PhPs, especially at $\phi = 90°$. Furthermore, as different graphene layers are added at the top or bottom of α-MoO_3 in α-MoO_3/VO_2 structure, actively tunable HPPPs inside its RBs and SPPPs outside the RBs are realized via the coupled function between α-MoO_3 PhPs and graphene SPPs. In addition, actively tunable SE enhancement of α-MoO_3 can be realized via controlling the VO_2 phase transition and the graphene chemical potential. The high susceptibility of PhPs of α-MoO_3 opens new possibilities for potential applications in combination with strongly correlated quantum materials including PCMs and graphene.

Acknowledgments

Project supported by the National Natural Science Foundation of China (Grant Nos. 52204258 and 52106099), the Postdoctoral Research Foundation of China (Grant No. 2023M743779), the Fundamental Research Funds for the Central Universities (Grant No. 2022QN1017), the Key Research Development Projects in Xinjiang Uygur Autonomous Region (Grant No. 2022B03003-3), and the Shandong Provincial Natural Science Foundation (Grant No. ZR2020LLZ004).

References

[1] Poddubny A, Iorsh I, Belov P and Kivshar Y 2013 *Nat. Photon.* **7** 948
[2] Drachev V P, Podolskiy V A and Kildishev A V 2013 *Opt. Express* **21** 15048
[3] Smith D and Schurig D 2003 *Phys. Rev. Lett.* **90** 077405
[4] Wu X, McEleney C A, González-Jiménez M and Macêdo R 2019 *Optica* **6** 1478
[5] Wu X and Fu C 2021 *Int. J. Heat Mass Transfer* **168** 120908
[6] Liu R, Zhou C, Zhang Y, Cui Z, Wu X and Yi H 2022 *Int. J. Extreme Manufact.* **4** 032002
[7] Ma W, Alonso-González P, Li S, Nikitin A Y, Yuan J, Martín-Sánchez J, Taboada-Gutiérrez J, Amenabar I, Li P and Vélez S 2018 *Nature* **562** 557
[8] Zheng Z, Chen J, Wang Y, Wang X, Chen X, Liu P, Xu J, Xie W, Chen H and Deng S 2018 *Adv. Mater.* **30** 1705318
[9] Zheng Z, Xu N, Oscurato S L, Tamagnone M, Sun F, Jiang Y, Ke Y, Chen J, Huang W and Wilson W L 2019 *Sci. Adv.* **5** eaav8690
[10] Ivarez-Pérez G, Folland T G, Errea I, Taboada-Gutiérrez J, Duan J, Martín-Sánchez J, Tresguerres-Mata A I, Matson J R, Bylinkin A and He M 2020 *Adv. Mater.* **32** 1908176
[11] Wu X and Liu R 2020 *ES Energy & Environ.* **10** 66
[12] Bapat A, Dixit S, Gupta Y, Low T and Kumar A 2022 *Nanophotonics* **11** 2329
[13] Liu H, Ai Q, Ma M, Wang Z and Xie M 2022 *Int. J. Therm. Sci.* **177** 107587
[14] Liu H, Hu Y, Ai Q, Xie M and Wu X 2022 *J. Appl. Phys.* **132** 175105
[15] Dai S, Zhang J, Ma Q, Kittiwatanakul S, McLeod A, Chen X, Corder S G, Watanabe K, Taniguchi T and Lu J 2019 *Adv. Mater.* **31** 1900251
[16] Zhou K, Lu L, Li B and Cheng Q 2021 *J. Appl. Phys.* **130** 093102
[17] Novoselov K S, Geim A K, Morozov S V, Jiang D E, Zhang Y, Dubonos S V, Grigorieva I V and Firsov A A 2004 *Science* **306** 666
[18] Fei Z, Rodin A, Andreev G O, Bao W, McLeod A, Wagner M, Zhang L, Zhao Z, Thiemens M and Dominguez G 2012 *Nature* **487** 82
[19] Ju L, Geng B, Horng J, Girit C, Martin M, Hao Z, Bechtel H A, Liang X, Zettl A and Shen Y R 2011 *Nat. Nanotechnol.* **6** 630
[20] Grigorenko A N, Polini M and Novoselov K 2012 *Nat. Photon.* **6** 749
[21] Bao Q and Loh K P 2012 *ACS Nano* **6** 3677
[22] Song J and Cheng Q 2016 *Phys. Rev. B* **94** 125419
[23] Kumar A, Low T, Fung K H, Avouris P and Fang N X 2015 *Nano Lett.* **15** 3172
[24] Zhou K, Cheng Q, Lu L, Li B, Song J and Luo Z 2020 *Opt. Express* **28** 1647
[25] Xu J, Cui X, Liu N, Chen Y and Wang H W 2021 *SmartMat* **2** 202
[26] Sun M, Zhang C, Chen D, Wang J, Ji Y, Liang N, Gao H, Cheng S and Liu H 2021 *SmartMat* **2** 213
[27] Zhou K, Cheng Q, Lu L, Li B, Song J, Si M and Luo Z 2020 *Appl. Opt.* **59** 595
[28] Song J, Cheng Q, Lu L, Li B, Zhou K, Zhang B, Luo Z and Zhou X 2020 *Phys. Rev. Appl.* **13** 024054
[29] Benkahoul M, Chaker M, Margot J, Haddad E, Kruzelecky R, Wong B, Jamroz W and Poinas P 2011 *Sol. Energy Mater. Sol. Cells* **95** 3504
[30] Choi H, Ahn J, Jung J, Noh T and Kim D 1996 *Phys. Rev. B* **54** 4621
[31] Soltani M, Chaker M, Haddad E, Kruzelecky R and Margot J 2004 *Appl. Phys. Lett.* **85** 1958
[32] Shibuya K, Kawasaki M and Tokura Y 2010 *Appl. Phys. Lett.* **96** 022102
[33] Lee S, Hippalgaonkar K, Yang F, Hong J, Ko C, Suh J, Liu K, Wang K, Urban J J and Zhang X 2017 *Science* **355** 371
[34] Tang K, Dong K, Li J, Gordon M P, Reichertz F G, Kim H, Rho Y, Wang Q, Lin C Y and Grigoropoulos C P 2021 *Science* **374** 1504
[35] Mlyuka N, Niklasson G A and Granqvist C-G 2009 *Sol. Energy Mater. Sol. Cells* **93** 1685
[36] Schubert M 1996 *Phys. Rev. B* **53** 4265
[37] Wu X, Fu C and Zhang Z M 2019 *Int. J. Heat. Mass. Transfer* **135** 1207
[38] Wu X, Su C, Shi K, Wu F and Fu C 2022 *Eng. Sci.* **19** 273
[39] Wu X, Fu C and Zhang Z 2018 *J. Photon. Energy* **9** 032702
[40] Sun Y, Wu B, Shi K, Shi Z and Wu X 2022 *Eng. Sci.* **20** 157
[41] Wu X, Fu C and Zhang Z M 2020 *J. Heat Transfer* **142** 072802
[42] Zhao B, Guizal B, Zhang Z M, Fan S and Antezza M 2017 *Phys. Rev. B* **95** 245437
[43] Purcell E M, Torrey H C and Pound R V 1946 *Phys. Rev.* **69** 37
[44] Ford G W and Weber W H 1984 *Phys. Rep.* **113** 195
[45] Debu D T, Ladani F T, French D, Bauman S J and Herzog J B 2019 *npj 2D Mater. Appl.* **3** 30
[46] Zhou K, Zhong X, Cheng Q and Wu X 2022 *Opt. Mater.* **131** 112623